IET Electric Power Applications

Research Article

IET Journals
The Institution of Engineering and Technology

Efficiency improvement and torque ripple minimisation of four-phase switched reluctance motor drive using new direct torque control strategy

ISSN 1751-8660
Received on 24th May 2019
Revised 24th July 2019
Accepted on 29th August 2019
doi: 10.1049/iet-epa.2019.0432
www.ietdl.org

Pittam Krishna Reddy[1] ✉, *Deepak Ronanki*[2], *Parthiban Perumal*[1]

[1]*Department of Electrical and Electronics Engineering, National Institute of Technology Karnataka, Surathkal 575 025, India*
[2]*Department of Electrical and Computer Engineering, University of Ontario Institute of Technology, Oshawa, Ontario L1G 0C5, Canada*
✉ *E-mail: krishnareddy4308@gmail.com*

Abstract: The direct torque control (DTC) strategy is one of the most effective techniques, used to control the switched reluctance motor (SRM) with improved dynamic performance and reduced torque ripple. However, this approach draws a higher source current due to an extension of the phase current into the negative torque region, which lowers the net torque per ampere ratio. This study proposes a new DTC strategy for SRM to overcome this issue by modifying the partition of the sectors and appropriate voltage vector selection. Therefore, the proposed method improves the drive efficiency while minimising torque ripple. To implement this method, a non-linear machine model is developed using the torque and flux characteristics obtained from experimental studies on a four-phase 8/6 SRM. The proposed DTC scheme is implemented on a digital control platform and power loss calculations are performed to evaluate the drive efficiency. Test results show that the proposed DTC method has improved performance in terms of efficiency and torque ripple under various operating conditions in comparison to the conventional DTC strategy.

1 Introduction

Non-availability and price volatility of rare-earth metals and permanent magnets has led research towards magnet free motor drive configurations that are more efficient, power dense and rugged to extreme environmental conditions [1]. The switched reluctance motor (SRM) is a strong contender to conventional motors due to its distinctive features of rugged construction, absence of permanent magnets, high starting torque with low starting current, low manufacturing cost, wide speed range with more field weakening region and inherent fault-tolerance [2, 3]. Due to these distinctive features, SRMs are exceptionally attractive and have become a prominent candidate in industrial, residential, commercial, and transportation sectors such as electrified vehicles [3, 4], integrated motor drive and battery chargers [5, 6], renewable power systems [6–8], aircraft starter/generator [9, 10], and ultra-high-speed applications [11, 12].

However, it has some limitations such as high torque ripple, severe acoustic noise, and vibration and demands rotor position information for control, which causes a hindrance in the aforementioned applications. Furthermore, it is intractable to establish smooth torque control in the SRM due to the doubly salient structure and non-linear machine characteristics [13]. Over the past years, many investigations have been carried out to minimise the torque ripple, which is mainly through machine design optimisation and high-performance control strategies. The torque ripple reduction through machine design involves the optimisation of machine parameters such as pole shape, core, air gap, geometry modifications and winding arrangement [14–18].

Fundamentally, higher phase SRMs have an added advantage of reduced torque ripple, reduced phase current and enhanced fault-tolerance in comparison to three-phase SRMs [19]. For instance, torque ripple in the four-phase SRMs is 20% less than three-phase SRMs [20]. With continuing improvements in power electronics and packaging, the current trend is more towards the high-phase machines [21]. However, a further increase in phase number with the use of asymmetric half-bridge converter (AHB) increases the device component count, thus increasing the system cost and complicating the control algorithms. Thus, four-phase SRMs are widely used in various industrial, automotive and aviation applications [8, 20, 22].

Alternatively, torque ripple can be minimised using advanced or optimised control techniques such as current profiling techniques (CPTs) [23, 24] and torque sharing functions (TSFs) [25–27], where the torque is an indirect control variable. However, these methods necessitate dedicated tuning procedures to determine optimal gain coefficients, long settling time and high memory requirements to store machine characteristics which are undesirable features for the real-time implementation. On the other hand, direct torque control (DTC) techniques are proposed for SRM to overcome the aforementioned shortcomings, namely direct instantaneous torque control, direct torque and flux control and advanced DTC strategies [28–30]. In these methods, torque is a direct control variable and the performance comparison of different control strategies is presented in [31, 32].

Among them, the DTC scheme [29] draws more attention which utilises the principle of DTC applied to traditional AC machines. This method offers advantages such as automatic control (no turn-on/off angle control), fast dynamic response, reduced acoustic noise, insensitivity to motor parameters and does not require rotor position information. Moreover, this method does not require any winding arrangements and provides an easy extension to multi-phase SRMs. However, the active phase has to develop more torque to compensate for the negative torque generated by the outgoing phase due to an extension of phase current in the negative inductance slope region. Therefore, it draws more current from the source, thereby reducing net torque per ampere (T/A) and the drive efficiency [29, 31]. Moreover, the large input power pulsations occur, which demands a larger DC-link capacitor.

To overcome these limitations, a new DTC scheme for four-phase SRM to improve the drive efficiency while minimising the torque ripple is proposed in this paper. This method employs a new switching pattern, which is generated by dividing the space-vector structure into 16 sectors and the selection of the voltage vectors are modified to eliminate phase current extension into the negative inductance slope region. Therefore, the proposed scheme not only minimises torque pulsations but also enhances the efficiency of the SRM drive. The performance of the proposed DTC controller is

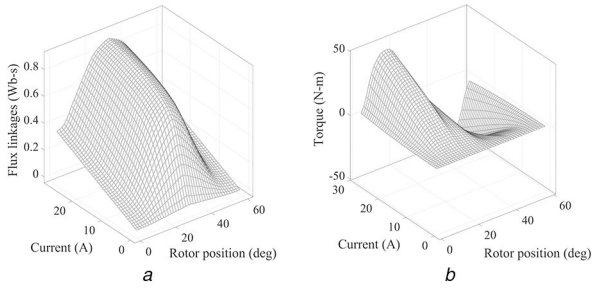

Fig. 1 *Torque and magnetic characteristics of 4 kW, 8/6 SRM obtained from experiments*
(a) Flux-linkage characteristics, ***(b)*** Torque characteristics

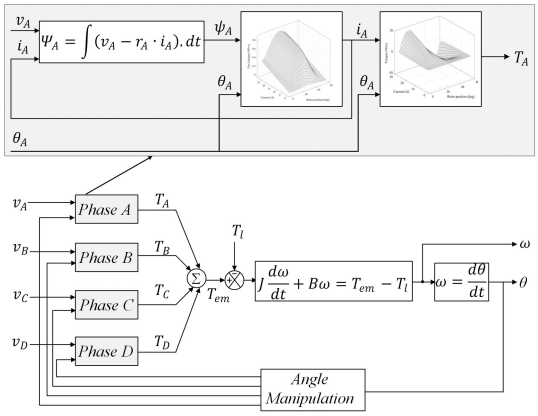

Fig. 2 *Dynamic model of four-phase SRM*

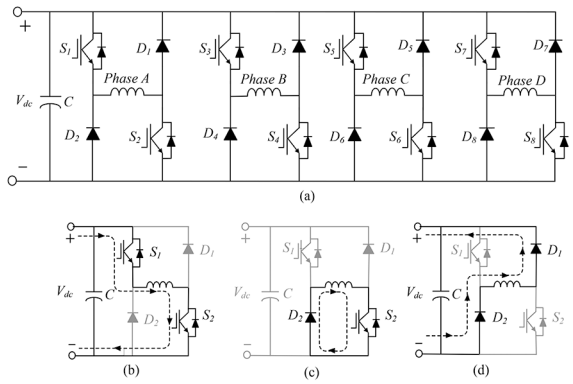

Fig. 3 *Power converter for four-phase SRM*
(a) Asymmetric Half-Bridge (AHB) converter, ***(b)*** Magnetising state (+1), ***(c)*** Freewheeling state (0), ***(d)*** Demagnetising state (−1)

validated against the conventional DTC controller under different operating conditions using simulations and in a real-time environment.

2 SRM drive

2.1 SRM modelling

The SRM has a doubly salient structure and operates in the saturation region in order to attain a high energy conversion rate, which makes it a highly non-linear machine. Therefore, it is necessary to develop an accurate and non-linear model for precise control of the SRM. Several modelling methods for the SRM are available in the literature, including finite element analysis based techniques, analytical methods and artificial intelligence techniques. In this paper, an interpolation and look-up table based approach is adopted using the torque and magnetic characteristics as shown in Fig. 1, which are obtained from experimental studies on 4 kW four-phase SRM. The dynamic model of an SRM comprises of a set of electrical equations for each phase and system dynamics. Neglecting mutual coupling, the SRM model of m-phase machine can be expressed as

$$v_j = r_j \cdot i_j + \frac{\mathrm{d}\psi_j(i_j,\theta_j)}{\mathrm{d}t}; \quad j = 1,2,\ldots,m$$
$$v_j = r_j \cdot i_j + \left(\frac{\partial \psi_j}{\partial i_j} \cdot \frac{\mathrm{d}i_j}{\mathrm{d}t}\right) + \left(\frac{\partial \psi_j}{\partial \theta_j} \cdot \frac{\mathrm{d}\theta_j}{\mathrm{d}t}\right) \tag{1}$$

The dynamic equation of the phase current can be expressed as

$$\frac{\mathrm{d}i_j}{\mathrm{d}t} = \left[\frac{\partial \psi_j}{\partial i_j}\right]^{-1} \cdot \left[v_j - r_j \cdot i_j - \frac{\partial \psi_j}{\partial \theta_j} \cdot \omega\right] \tag{2}$$

where v_j, i_j, r_j, ψ_j, and θ_j represent the terminal voltage, phase current, phase winding resistance, flux linkages, rotor position of 'j' phase, respectively and $\omega = \mathrm{d}\theta/\mathrm{d}t$ is the rotor speed. The general expression of the instantaneous torque by one phase at any rotor position can be expressed as

$$T_j = \left.\frac{\partial W_{\mathrm{c}}(i_j,\theta)}{\partial \theta}\right|_{i_j = \text{constant}} \tag{3}$$

where $W_{\mathrm{c}}(i_j,\theta)$ denotes co-energy, which can be given by

$$W_{\mathrm{c}} = \int_0^i \psi_j(i_j,\theta) \cdot \mathrm{d}i \tag{4}$$

The expression for instantaneous torque T_j can be given by

$$T_j \simeq i_j \cdot \frac{\partial \psi_j(i_j,\theta)}{\partial \theta} \tag{5}$$

The dynamics of the mechanical system is represented by

$$\frac{\mathrm{d}\omega}{\mathrm{d}t} = \frac{1}{J}\left[\sum_{j=1}^{m} T_j(i_j,\theta_j) - T_L - B \cdot \omega\right] \tag{6}$$

The SRM model is developed [33] using the above dynamic equations and the machine characteristics (Fig. 1). The complete SRM model with the per-phase model is shown in Fig. 2.

2.2 Power converter

The AHB is a widely used power converter topology to drive the SRM, as it allows independent control of each phase. The electric circuit diagram, along with their operating modes for the four-phase SRM is shown in Fig. 3*a*–*d*. One H-bridge module is required to drive one-phase of the SRM, which comprises of two power switching devices [S_1, S_2], and diodes [D_1, D_2] and the phase winding is connected in series with the power switches. There are three possible states that can be achieved through an AHB to drive the SRM. The positive dc voltage ($+V_{\mathrm{dc}}$) is applied across the phase winding when both switches in the same phase leg are turned on as shown in Fig. 3*b*, represents magnetisation state and is denoted by '1'. The freewheeling state can be achieved by turning off one of the switches as shown in Fig. 3*c*, that applies zero voltage across switch, which is denoted by '0'. To decrease the current abruptly, both switches are turned-off as shown in Fig. 3*d*. In this mode, negative dc voltage is applied across the winding leading to commutation of a phase. This state is called demagnetisation mode and is represented as '−1'. The summary of the possible voltage states for phase-A is listed in Table 1.

3 Proposed DTC scheme

The DTC strategies are very popular for conventional AC machines and have been applied to the SRM [29]. The principle of vector selection in DTC involves acceleration and deceleration of the flux linkage vector to compensate torque and flux errors.

Furthermore, the torque control of an SRM depends only on the stator flux vector's variation, thus no need for motor information. The control block diagram of the DTC scheme for an SRM is shown in Fig. 4. The DTC structure comprises of flux-linkage

Table 1 Operating modes of four-phase SRM converter (AHB)

S_1	S_2	D_1	D_2	State
1	1	0	0	magnetising state (+1)
1	0	1	0	freewheeling state (0)
0	1	0	1	freewheeling state (0)
0	0	1	1	demagnetising state (−1)

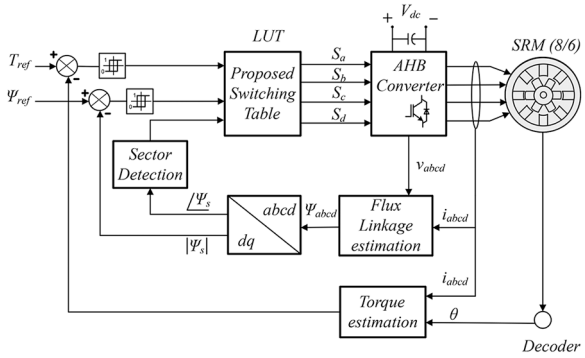

Fig. 4 *Block diagram of the proposed DTC scheme*

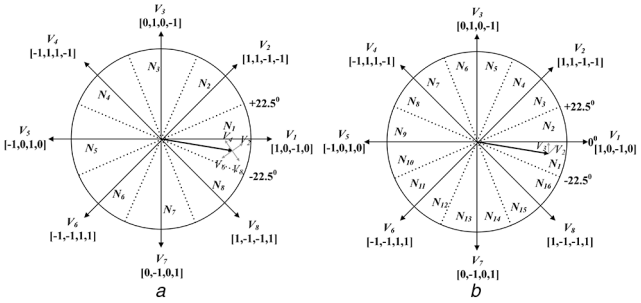

Fig. 5 *Sector partition and voltage vector selection for the sector* N_1
(a) Conventional DTC, ***(b)*** Proposed DTC

control, torque control and a flux-linkage vector's position information to choose voltage vector such that the desired torque control is achieved. In the conventional DTC scheme, total electrical space is divided into eight sectors with an angle of 45°, as shown in Fig. 5*a*. The selection of the voltage vectors based on the increment and decrement of torque and flux for conventional DTC is shown in Fig. 6*a*. The stator flux-linkage vector can be estimated as

$$\boldsymbol{\psi}_j = \int_0^t (\boldsymbol{v}_j - r_j \boldsymbol{i}_j) \cdot \mathrm{d}t + \boldsymbol{\psi}_{jo} \tag{7}$$

where $\boldsymbol{\psi}_{jo} = 0$ as the phase current and flux returns to zero in each electrical cycle in SRM. To evaluate the stator flux-linkage vector, the flux vectors for four-phase SRM are transformed into the *d–q* reference axes

$$\left.\begin{aligned} \boldsymbol{\psi}_s &= \boldsymbol{\psi}_d + j\boldsymbol{\psi}_q \\ |\psi_s| &= \sqrt{\psi_d^2 + \psi_q^2} \\ \theta &= \tan^{-1}\left(\frac{\psi_q}{\psi_d}\right) \end{aligned}\right\} \tag{8}$$

where $|\psi_s|$, θ represents the flux-linkage vector's magnitude and angle, which is used to determine the sector N_k ($k \in \{1, 2, \ldots, 8\}$). The torque can be estimated through the measurements by torque sensor or pre-determined torque characteristics of the motor.

Fundamentally, the SRM windings are to be excited in conjunction to phase inductance variation with respect to the rotor position. The determination of optimal switching pattern is crucial to achieving objectives such as minimal torque pulsations, high T/A ratio and reduced switching frequency. The conventional DTC switching pattern does not follow the phase inductance variation; as a result it generates high torque ripple and draws high source current to generate the required electro-magnetic torque, that lowers the efficiency of the drive. As discussed before, the torque can be increased by accelerating the flux linkage vector causing the incoming phase to conduct in the positive torque region, so that the requirement can be fulfilled. Similarly, the torque can be decreased by magnetising the outgoing phase, which is in the negative torque region, which is at the cost of increased commutations, lower T/A and more switching losses. Furthermore, large input power pulsations occur which is undesirable, especially for applications such as battery-powered electric vehicles.

All these issues are due to inappropriate voltage vector selection while decreasing torque. This issue can be overcome by proposing a new DTC strategy with a new sector partition method and switching sequence. In this scheme, magnetisation of the outgoing phase is replaced with freewheeling/demagnetisation of the active phase. A sixteen sector partition method with an electrical angle of 22.5° is employed instead of the eight sector approach, as shown in Fig. 5*b*, which allows precise selection of voltage vectors corresponding to torque and flux errors. Furthermore, the voltage vectors at +90° and −90° are selected to increase the torque ($T \Uparrow$) and decrease the torque ($T \Downarrow$) to achieve a faster dynamic response, which is not possible in the conventional DTC scheme, each sector occupies 45° of flux-linkage vector. In the proposed DTC method, if the flux-linkage vector is in sector N_1, the range of phase lead is 67.5°– 45°. At 0° position, the voltage vector selection to increase torque will change from V_2 to V_3, which leads the flux-linkage vector by 90°. At the end of sector N_2 (22.5°), the voltage vector leads the flux-linkage vector by 67.5°. In this way, the changing of vector selection for every 22.5° allows selection of the most appropriate voltage vectors such that fast dynamic response with low torque pulsations is achieved.

The selection of the voltage vectors using the proposed DTC scheme is presented in Fig. 6*b*. The proposed method utilises the new vectors for a decrease in torque by replacing all magnetisation (1) modes with freewheeling modes (0), thus eliminating the negative torque production. Furthermore, the proposed DTC scheme avoids all (−1) to (+1) switching transitions, i.e. the switching of an AHB converter from demagnetisation mode (−1) to magnetisation mode (+1) involves switching of both switches of a particular phase, whereas magnetisation to freewheeling transition involves only one switch. Therefore, soft chopping with single switch transition can also be achieved using the proposed method. The main features of the proposed DTC scheme are summarised as

i. Avoids the stability concerns due to minimal torque pulsations.
ii. Improves T/A ratio and reduces copper losses.
iii. Reduces the number of switching commutations, thereby offers low converter switching losses.
iv. Reduces input current fluctuations, thus enhances the battery life.

4 Results and discussion

The performance and effectiveness of the proposed DTC scheme are first verified through computer simulations. The simulation studies are carried out on 4-kW four-phase SRM using MATLAB/ Simulink. The magnetisation and static torque characteristics obtained from the experimental measurements are used to develop a non-linear dynamic model of SRM. The results obtained using the proposed scheme under steady-state as well as dynamic conditions are illustrated and compared with the conventional DTC. Figs. 7 and 8 show the simulated waveforms of the proposed and conventional DTC strategies for a reference torque of $T_{\mathrm{ref}} = 15\,\mathrm{N-m}$ at 250 and 750 rpm, respectively. From these results, we can also observe that the extension of the phase current and negative phase torque that exists in conventional DTC is completely eliminated in the SRM drive using the proposed DTC strategy. Moreover, the torque dips observed during the phase commutation in the conventional DTC are shown in Figs. 7*b* and 8*b*. These torque dips are reduced using the proposed DTC as

depicted in Figs. 7*a* and 8*a*. Thus, the desired torque is well regulated at their reference value with an improved T/A ratio using the proposed DTC strategy and outperforms the conventional DTC strategy in terms of torque ripple and T/A ratio under low and high speeds.

The dynamic performance of the SRM drive with the proposed DTC scheme is validated by changing the torque reference during acceleration and declaration modes. As shown in Fig. 9, torque reference (T_{ref}) changed from 10 to 15 N-m at 1 s and from 15 to 5 N-m at 1.2 s. It is observed that the SRM drive is able to track the

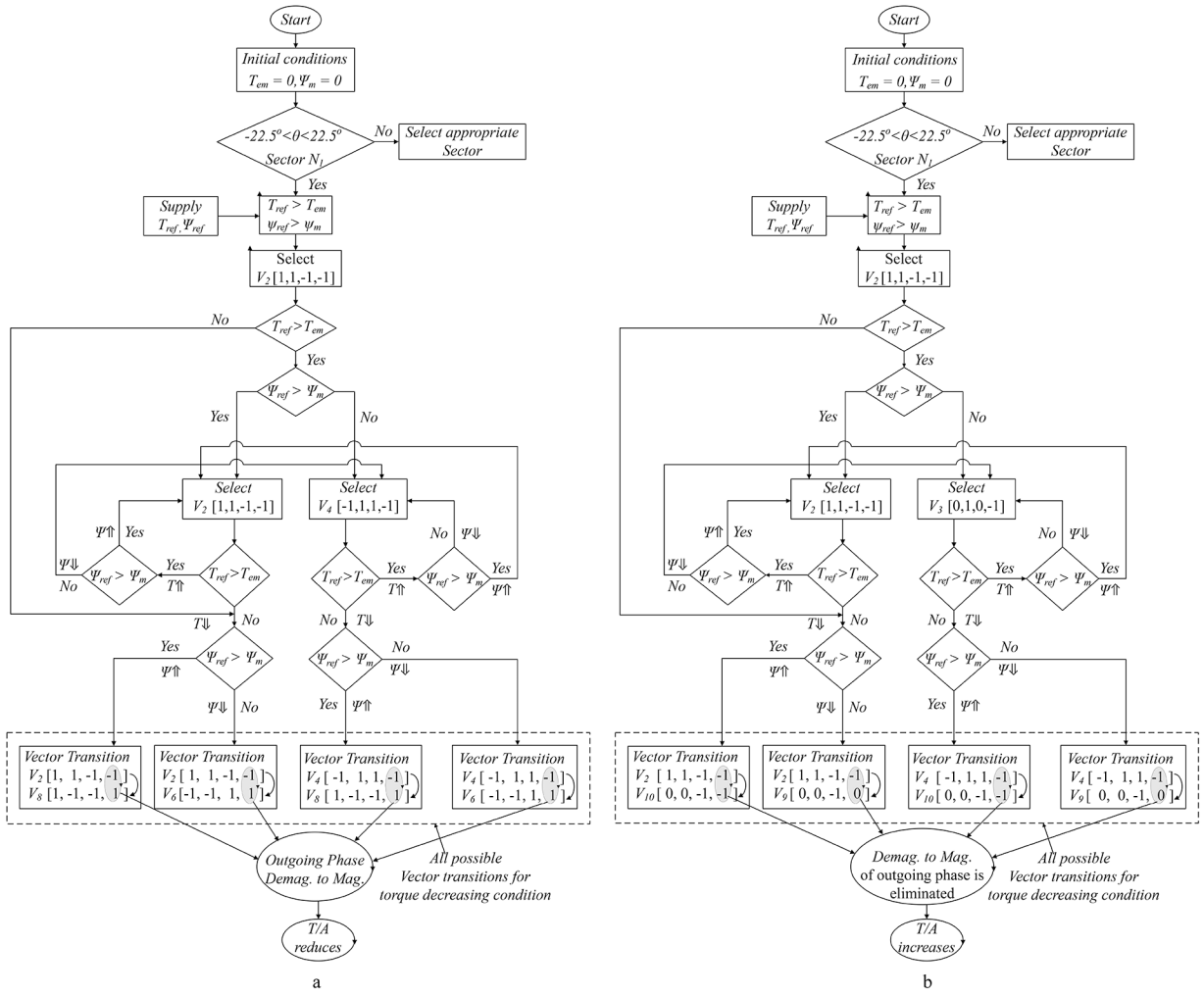

Fig. 6 *Flowchart of the DTC strategies*
(a) Conventional DTC, ***(b)*** Proposed DTC

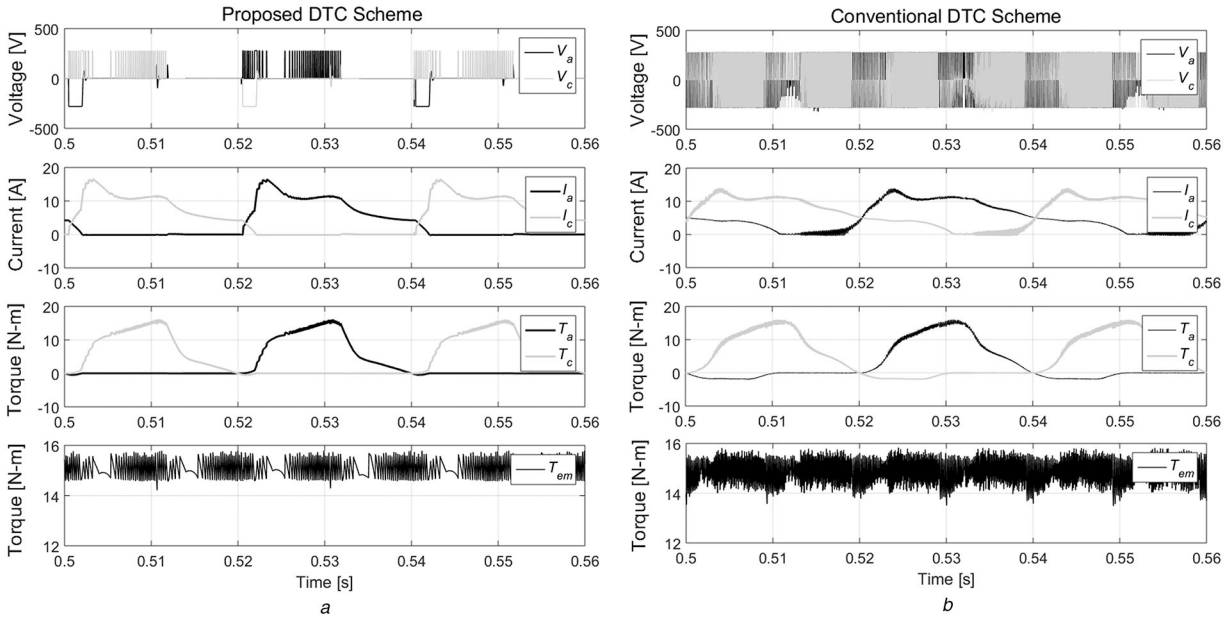

Fig. 7 *Steady-state simulation results of four-phase SRM at 250 rpm*
(a) Proposed DTC, ***(b)*** Conventional DTC

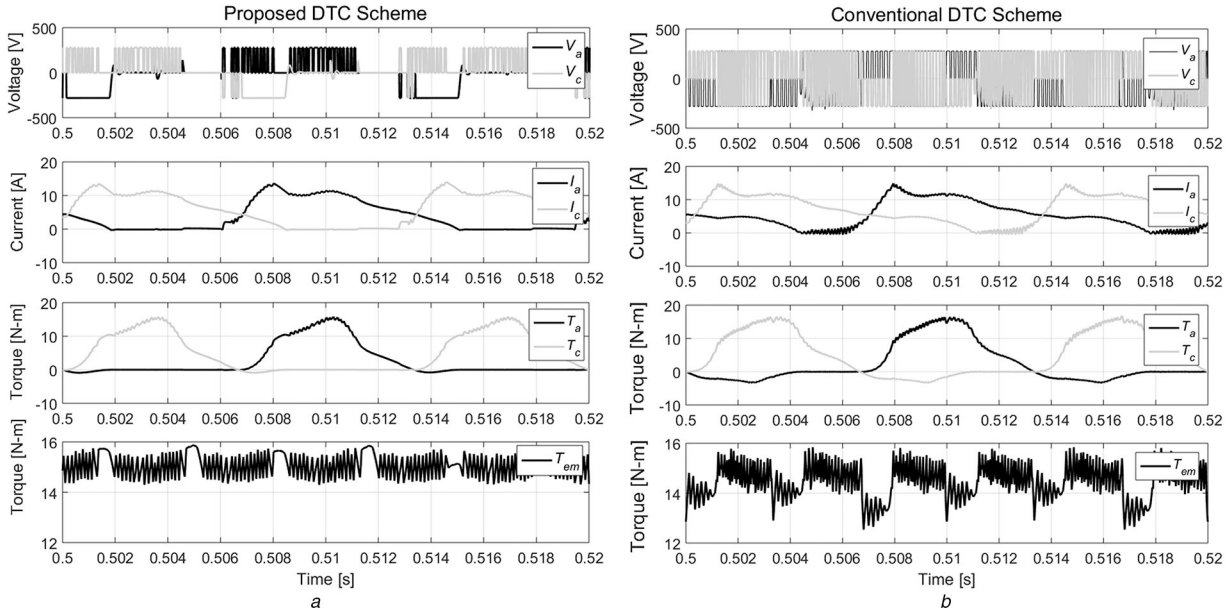

Fig. 8 *Steady-state simulation results of four-phase SRM at 750 rpm*
(a) Proposed DTC, ***(b)*** Conventional DTC

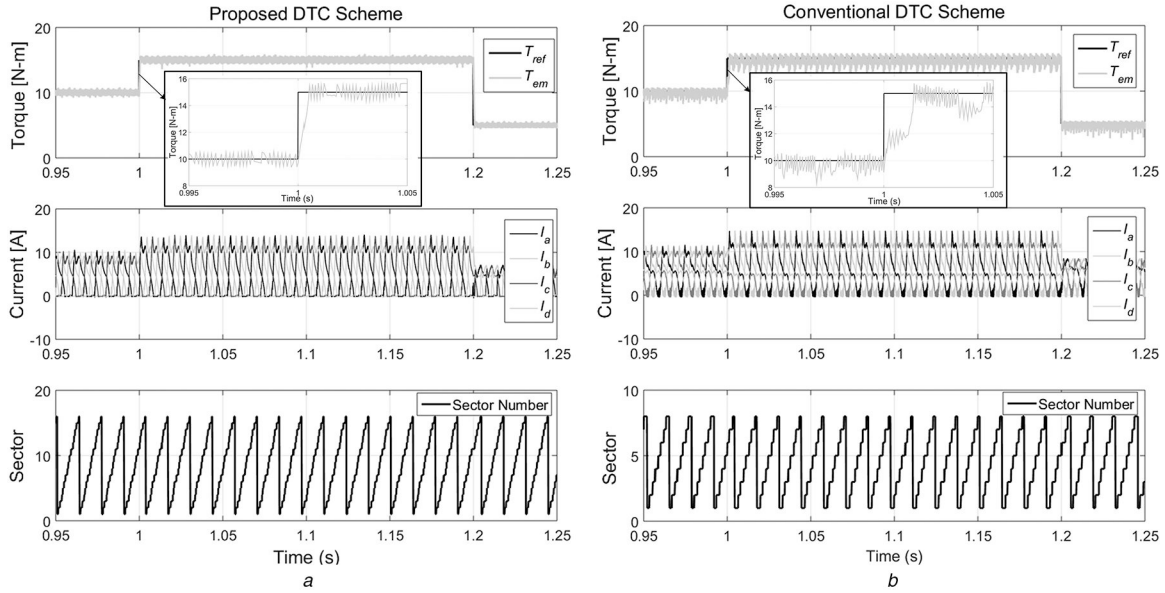

Fig. 9 *Dynamic performance of four-phase SRM at 750 rpm*
(a) Proposed DTC, ***(b)*** Conventional DTC

T_{ref} effectively in comparison to the conventional DTC, as shown in Fig. 9. This is due to selecting vectors which are orthogonal to the stator flux linkage vector. The dynamic response of conventional DTC has a delay in settling as well as the undershoots at the new reference torques. Therefore, the proposed DTC strategy exhibits fast dynamic performance with reduced torque pulsations under different torque references. Furthermore, the prediction error for estimating rotor position is minimised due to the sixteen-sector partition method, which helps to detect accurate flux vector information.

The conventional DTC strategy is also verified through real-time studies. The proposed and conventional DTC schemes are implemented on an OPAL-RT-based digital controller (OP5142) with 50 μs sampling time. The four-phase SRM model under study is developed using experimental torque and magnetic characteristics following the methodology in [34]. With the application of dc voltage, the current waveforms are captured at each rotor position (from unaligned to aligned). The dividing head is used to lock the rotor at each position against the torque produced. The measured voltages and currents are further processed into a simulation platform to calculate flux linkages using (7). The motor parameters and the testing conditions of a real-time system are similar to the simulation studies. The real-time results shown in Figs. 10*a* and *b* are found to be in concurrence with the corresponding MATLAB simulation results in terms of electro-magnetic torque, phase torque, phase current and rotor angle. As shown in Fig. 10*b*(i), the extension of the phase current and phase negative torque are completely eliminated under the negative inductance slope region. Thus, the proposed drive improves *T*/*A* in the SRM drive, thereby enhancing the drive efficiency.

The gating pulse of devices S_1 and S_2 [Fig. 3] using both techniques are shown in Figs. 10*a* and *b*(ii). This study reveals that the number of switching as well as device voltage stress are less in the proposed DTC strategy in comparison to conventional DTC for the fundamental cycle. Therefore, the average switching frequency of the SRM drive reduces significantly. From the presented results, it is concluded that the proposed DTC method outperforms under steady-state and dynamic conditions in comparison to the conventional DTC strategy. However, it is essential to conduct further studies on a proposed drive in terms of copper losses,

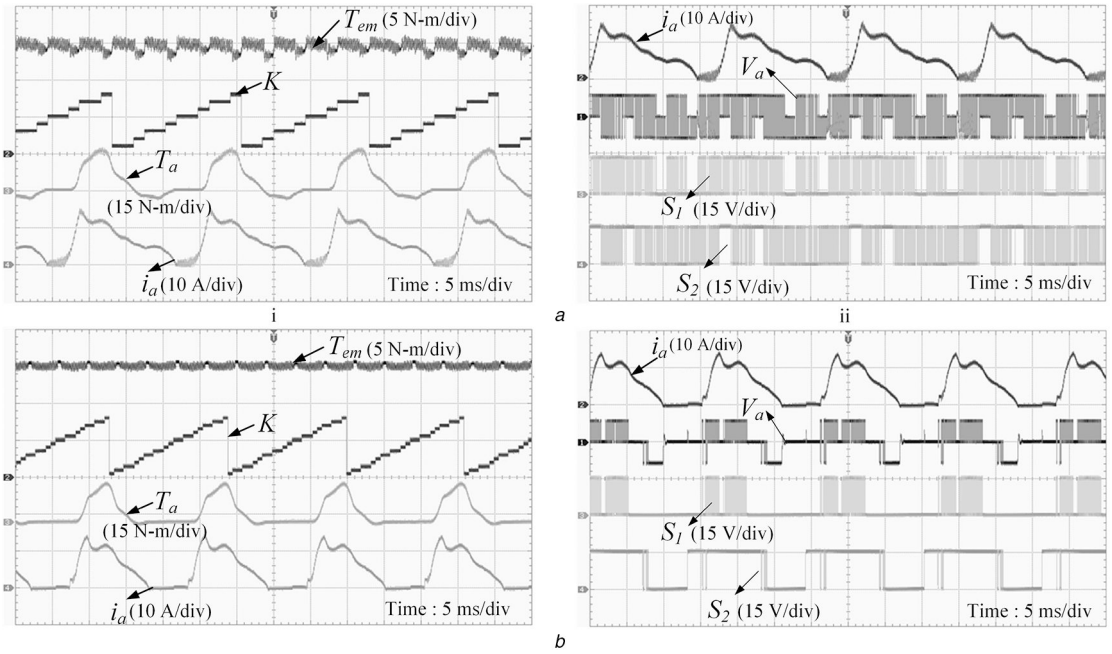

Fig. 10 *Real-time results at 750 rpm: Scope-i: CH_1: Total torque (N-m), CH_2: Sector number, CH_3: Phase-torque (N-m) and CH_4: Phase-current (A); Scope-ii: CH_1: Phase-current (A), CH_2: Phase-voltage (V), CH_3: Gate signal for S_1 and CH_4: Gate signal for S_2; Time scale: 5 ms/div*
(a) Conventional DTC scheme, ***(b)*** Proposed DTC scheme

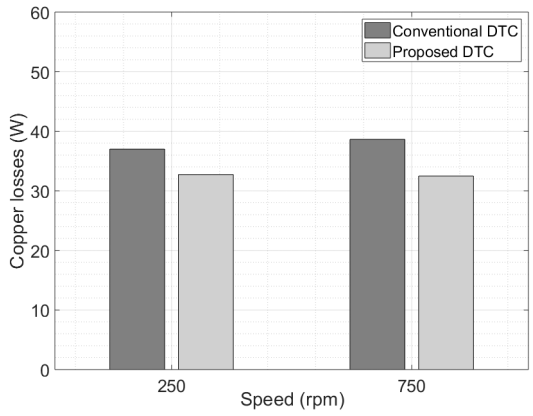

Fig. 11 *Comparison of per-phase copper losses under the conventional and proposed DTC schemes*

converter losses and the impact on the source current, which will be discussed in Section 5.

5 Performance analysis of DTC schemes

5.1 Torque ripple analysis

Toque dip occurs at the point of overlap during phase commutation, which is usually expressed in the form of torque ripple and is given by

$$T_{\text{ripple}}(\%) = \frac{T_{\max} - T_{\min}}{T_{\text{avg}}} \times 100\% \tag{9}$$

where T_{avg} can be expressed as

$$T_{\text{avg}} = \frac{1}{T}\int_0^T \left(\sum_{j=1}^{m} T_j(i_j, \theta_j)\right) \cdot \mathrm{d}t \tag{10}$$

Torque ripple is evaluated using (9) under both the DTC schemes at low and high speeds. With the application of the proposed DTC scheme, torque dips are reduced significantly during phase commutation as depicted in Figs. 7*a*, 8*a* and 10*b*(i). It is also observed that 32 and 36% torque ripple reduction using the proposed DTC based SRM drive at 250 and 750 rpm, respectively.

5.2 T/A and copper loss

The magnitude of the phase current in the inductance-decreasing region determines the amount of generated negative phase torque. The proposed DTC scheme eliminates completely phase current in the negative torque region, thereby improves the drive efficiency. In the case of SRM drives, it is usually expressed in terms of *T/A* [χ] and is given by

$$\chi = \frac{T_{\text{avg}}}{I_{\text{dc-avg}}} \tag{11}$$

where $I_{\text{dc-avg}}$ is the average value of the source current. It is observed that the proposed DTC scheme improves *T/A* ratio by 49.59 and 17.54% at 250 and 750 rpm, respectively. The copper losses can be evaluated as follows:

$$P_{\text{c}} = \sum_{j=1}^{m} (i_{j\text{rms}}^2 \cdot r_j) \tag{12}$$

where r_j is the phase AC resistance and $i_{j\text{rms}}$ is the r.m.s value of the jth phase current. Copper losses are determined using (12) for both schemes under different speeds. The performance analysis of both schemes in terms of copper losses is shown in Fig. 11. It is noticed that the copper losses are reduced by 11.56 and 15.92% using the proposed drive at 250 and 750 rpm, respectively.

5.3 Current stress on power devices and the number of commutations

Power devices have been found to be the most fragile components and are prone to fail due to varied current and voltage stress [35]. Therefore, it is essential to analyse stress on the devices that are subjected to different control strategies. Figs. 12 and 13 show the current distribution on each device of AHB per phase under the conventional and proposed DTC strategies at 750 rpm, respectively. It is observed that the switching of the devices is significantly reduced. Alternatively, it can also be analysed through the number of commutations in one electrical period. The number of commutations of the switch for one electrical cycle can be calculated using a digital counter circuit. In this method, the counter is incremented by one whenever the rising edge of the gate signal is detected. The difference between the counter count at the

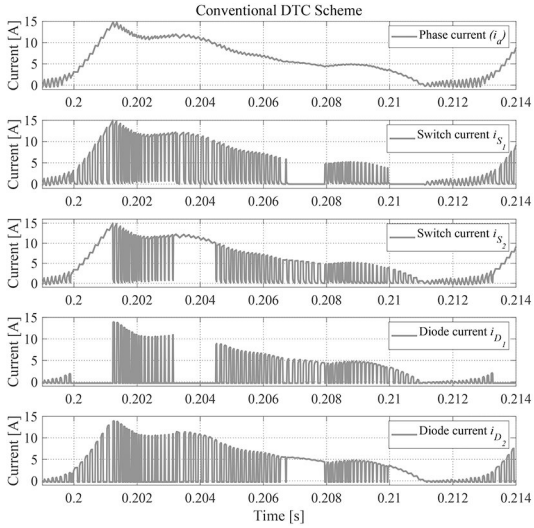

Fig. 12 *Device current stress under the conventional DTC scheme*

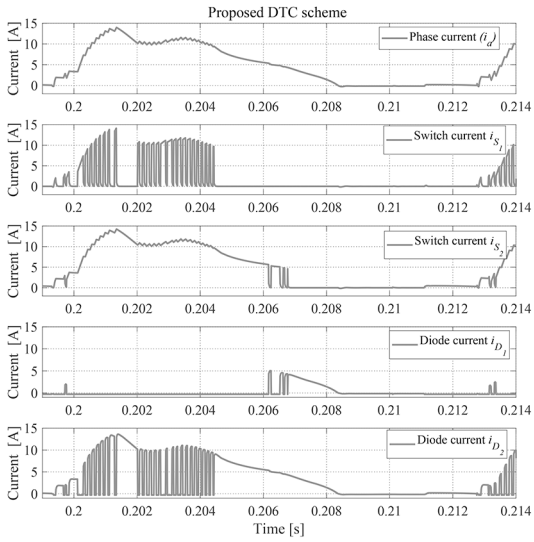

Fig. 13 *Device current stress under the proposed DTC scheme*

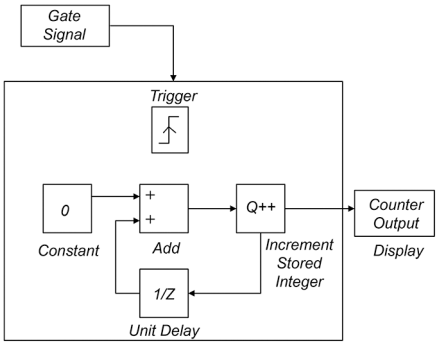

Fig. 14 *Block diagram of evaluating the number of commutations*

starting point and endpoint of the cycle gives the number of commutations. The block diagram of the digital count to evaluate the number of commutations per switch is shown in Fig. 14. Both per-phase active devices (S_1 and S_2) are switched 43 and 32 times in one-fundamental cycle of the proposed DTC method, whereas in conventional DTC both devices are switched 587 and 177 times at 250 and 750 rpm, respectively. The lesser number of commutations implies lower switching losses of the converter, which is observed in both simulation and real-time results. Therefore, average switching frequency of the proposed SRM drive is significantly reduced in comparison to the conventional DTC-based drive.

5.4 Power loss analysis

It is shown that the number of commutations is limited using the proposed DTC scheme by eliminating the magnetisation of the phase in the negative torque region. Even though the number of commutations is reduced, the conduction time of power diodes increases. As already discussed the reduction in RMS current to generate same electromagnetic torque reduces the converter conduction losses. Therefore, it is required to evaluate the power loss of the AHB converter. The total power losses P_{Total} of per-phase AHB are given by

$$P_{\text{Total}} = P_{L-S_1} + P_{L-D_1} + P_{L-S_2} + P_{L-D_2} \tag{13}$$

where P_{L-S_1}, P_{L-D_1}, P_{L-S_2} and P_{L-D_2} are the power losses of the upper switch, upper diode, lower switch and lower diode, respectively. The total power loss of a power switching device (S) and diode (D) is the sum of conduction losses and switching losses (turn-on loss and turn-off loss/recovery loss). The conduction loss of the switch/diode can be given by

$$P_{\text{cond},S/D} = \frac{1}{T}\int_0^T V_{\text{on},S/D} \times i(t)\text{d}t \tag{14}$$

The conduction loss of ($P_{\text{cond},S/D}$) switch and diode can be calculated from their forward voltage drop ($V_{\text{on},S/D}$) and their instantaneous current $i(t)$. The device characteristics are developed using the curve-fitting tool in the MATLAB by considering the electrical and thermal characteristics of Semikron IGBT SKM75GAL123D/SKM75GAR123D for one phase of AHB. The derived conduction loss equations of the switch (S) and diode (D) from the curve fitting analysis are listed as

$$P_{S,25^\circ\text{C}} = 0.02365 * i_S(t)^2 + 1.551 * i_S(t) - 0.8995 \tag{15}$$

$$P_{S,125^\circ\text{C}} = 0.02876 * i_S(t)^2 + 1.914 * i_S(t) - 2.452 \tag{16}$$

$$P_{D,25^\circ\text{C}} = 0.01521 * i_D(t)^2 + 1.245 * i_D(t) - 0.2321 \tag{17}$$

$$P_{D,125^\circ\text{C}} = 0.01485 * i_D(t)^2 + 1.06 * i_D(t) - 0.8451 \tag{18}$$

The second-order polynomial equations are developed for conduction power losses at temperatures (T) are given by

$$\begin{aligned} P_S(i_c, T) = {} & (0.0224 + 0.000058 * T) * i_S(t)^2 + (1.46025 \\ & + 0.00363 * T) * i_S(t) - (0.511375 + 0.015525 * T) \end{aligned} \tag{19}$$

$$\begin{aligned} P_D(i_D, T) = {} & 0.0153 * i_D(t)^2 + (1.2913 - 0.0019 * T) \\ & * i_D(t)(0.0789 + 0.0061 * T) \end{aligned} \tag{20}$$

The conduction losses are calculated using (14)–(20) as per methodology, as shown in Fig. 15*a*.

The switching losses of the switch ($S \rightarrow$ IGBT) and diode (D) are

$$P_{\text{Sw-S}} = \frac{1}{T}\sum_{j=1}^{N}[E_{\text{on}}(j) + E_{\text{off}}(j)] \tag{21}$$

$$P_{\text{Rec-D}} = \frac{1}{T}\sum_{j=1}^{N}[E_{\text{rec}}(j)] \tag{22}$$

where E_{on} and E_{off} are the turn-on and turn-off energies of switch, respectively. E_{rec} represents the recovery energy of the diode. The datasheet provides E_{on}, E_{off} and E_{rec} losses versus switch/diode current curves that describe the current dependency of switching losses. Other dependent factors of switching losses are blocking voltage and junction temperature. The switching loss factor can be

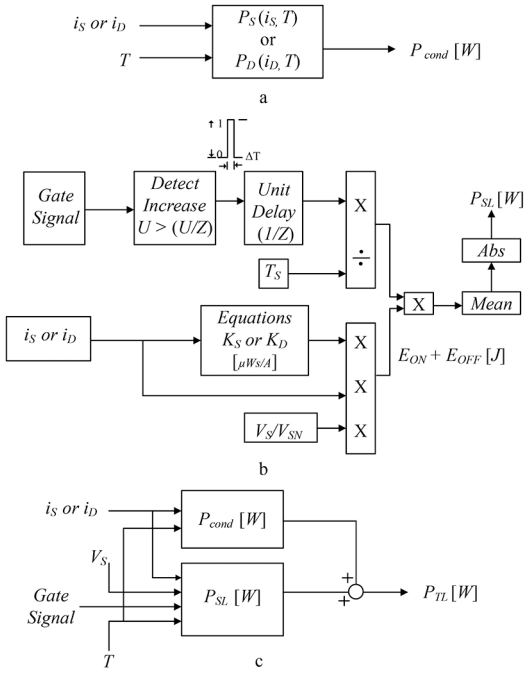

Fig. 15 *Block diagram of power loss evaluation methodology*
(a) Conduction losses, ***(b)*** Switching losses, ***(c)*** Total losses

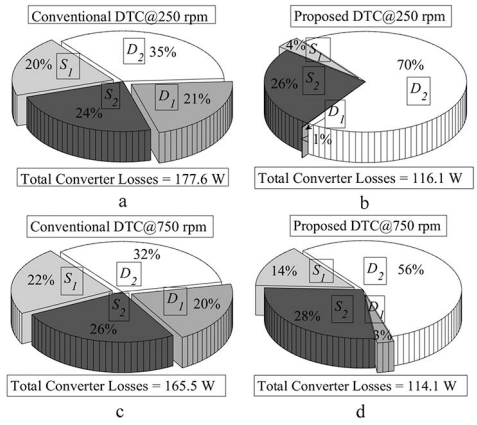

Fig. 16 *Converter power loss analysis*
(a) Conventional DTC at 250 rpm, ***(b)*** Proposed DTC at 250 rpm, ***(c)*** Conventional DTC at 750 rpm, ***(d)*** Proposed DTC at 750 rpm

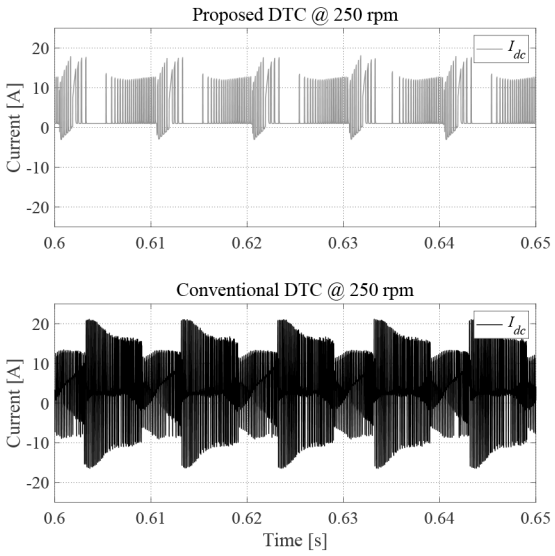

Fig. 17 *Comparison of source current I_{dc} using both DTC schemes at 250 rpm*

obtained by dividing total energy losses with switch/diode current can be represented as

$$K_{S/D} = \frac{E_{\text{total}}}{I_{S/D}} (\mu\text{Ws/A}) \tag{23}$$

The derived polynomial equations for switching loss factor from the selected switch datasheet are expressed as

$$K_S(i_S) = 0.0001487 * i_S(t)^3 - 0.03366 * i_S(t)^2 + 3.224 * i_S(t) + 170.3 \tag{24}$$

$$K_D(i_D) = -0.0007726 * i_D(t)^2 - 0.436 * i_D(t) + 65.53 \tag{25}$$

$K_S(i_S)$ is the switching loss factor of IGBT and $K_D(i_D)$ is the switching loss factor of a diode. The switching loss evaluation methodology adopted is shown in Fig. 15*b*. Once the conduction and switching losses are calculated, then the total losses for all devices are evaluated as shown in Fig. 15*c* [36]. The converter loss distribution comparison of the conventional and the proposed DTC strategies at 250 and 750 rpm are shown in Fig. 16.

5.5 Input power fluctuations

Due to non-linear characteristics and phase commutation of SRM, there are large input power fluctuations when transferring energy from the dc source to the SRM. This essentially arises movement from unaligned to aligned rotor position. Therefore, large current fluctuations occur at the input side considering the stiff dc source. In battery-powered electric vehicles, the battery lifetime is highly influenced by the ripple current [37]. One way to avoid such power fluctuations, is the use of large capacitors parallel with the battery. In order to compare the performance of both schemes, the same capacitor value is considered and their results at 250 rpm are shown in Fig. 17. It is observed that the proposed method reduces fluctuations in the source current, which improves the life of the battery in the battery-powered electrified vehicles.

5.6 Comparison summary of the proposed DTC scheme with conventional DTC

The comparison summary between these methods in terms of torque ripple, torque per ampere, source current and number of commutations are listed in Table 2. Overall, the proposed DTC method outperforms the conventional DTC method especially at lower speeds. The comparative analysis between the proposed DTC and the conventional DTC are summarised in Table 3.

6 Conclusion

In this paper, a new DTC algorithm for a four-phase SRM drive with improved efficiency is proposed. In this scheme, a sixteen-sector partition method is employed and the most appropriate voltage vectors are selected to regulate the desired torque with minimal torque pulsations. The proposed strategy effectively eliminates the instantaneous negative torque generated by the outgoing phase during phase commutation. Thus, the net *T/A* ratio is significantly increased and the torque ripple is minimised. To validate and implement the proposed control algorithm in real-time, a non-linear model is developed. The real-time results show that the proposed DTC scheme improves the drive efficiency in comparison to the conventional DTC scheme.

7 Acknowledgment

The authors thank Dr. M. Rajesh for helping us to obtain the torque and flux characteristics of 8/6 SRM through experiments.

Table 2 Performance comparison of the proposed DTC and conventional DTC scheme

Speed, rpm	Method	Torque ripple, %	*T/A* (avg), N-m/A	Source RMS current (I_s), A	Number of commutations (n)
250	proposed DTC	10.66	5.146	5.611	43
	conventional DTC	15.66	3.440	9.454	587
500	proposed DTC	13.66	3.438	7.311	39
	conventional DTC	19.20	2.648	9.627	309
750	proposed DTC	14.02	2.593	9.129	32
	conventional DTC	21.93	2.206	9.151	177

Table 3 Summary of comparative analysis of proposed and conventional DTC scheme

Scheme attributes	Conventional DTC [29]	Proposed DTC
sector partition method	eight	sixteen
voltage vectors used	eight	sixteen
torque ripple	high	low
T/A ratio	low	high
source current ripple	high	low
copper losses	high	low
switching losses	high	low
number of commutations	high	low
device current stress	high	low
device voltage stress	high	low
battery life	low	high
capacitor requirement	high	low
efficiency	low	high

8 References

[1] Boldea, I., Tutelea, L.N., Parsa, L., *et al.*: 'Automotive electric propulsion systems with reduced or no permanent magnets: an overview', *IEEE Trans. Ind. Electron.*, 2014, **61**, (10), pp. 5696–5711

[2] Chiba, A., Takano, Y., Takeno, M., *et al.*: 'Torque density and efficiency improvements of a switched reluctance motor without rare-earth material for hybrid vehicles', *IEEE Trans. Ind. Appl.*, 2011, **47**, (3), pp. 1240–1246

[3] Yang, Z., Shang, F., Brown, I.P., *et al.*: 'Comparative study of interior permanent magnet, induction, and switched reluctance motor drives for EV and HEV applications', *IEEE Trans. Transp. Electr.*, 2015, **1**, (3), pp. 245–254

[4] Chiba, A., Kiyota, K., Hoshi, N., *et al.*: 'Development of a rare-earth-free SR motor with high torque density for hybrid vehicles', *IEEE Trans. Energy Convers.*, 2015, **30**, (1), pp. 175–182

[5] Gan, C., Wu, J., Hu, Y., *et al.*: 'New integrated multilevel converter for switched reluctance motor drives in plug-in hybrid electric vehicles with flexible energy conversion', *IEEE Trans. Power Electron.*, 2017, **32**, (5), pp. 3754–3766

[6] Gan, C., Jin, N., Sun, Q., *et al.*: 'Multiport bidirectional SRM drives for solar-assisted hybrid electric bus powertrain with flexible driving and self-charging functions', *IEEE Trans. Power Electron.*, 2018, **33**, (10), pp. 8231–8245

[7] Ronanki, D., Parthiban, P.: 'PV-battery powered direct torque controlled switched reluctance motor drive'. Proc. IEEE Asia-Pacific Power and Energy Eng. Conf., Shanghai, People's Republic of China, 2012, pp. 1–4

[8] Narayana, V., Mishra, K.A., Singh, B.: 'Development of low-cost PV array-fed SRM drive-based water pumping system utilising CSC converter', *IET Power Electron.*, 2017, **10**, (2), pp. 156–168

[9] Bartolo, J.B., Degano, M., Espina, J., *et al.*: 'Design and initial testing of a high-speed 45-kW switched reluctance drive for aerospace application', *IEEE Trans. Ind. Electron.*, 2017, **64**, (2), pp. 988–997

[10] Shoujun, S., Weiguo, L., Peitsch, D., *et al.*: 'Detailed design of a high speed switched reluctance starter/generator for more/all electric aircraft', *Chin. J. Aeronaut.*, 2010, **23**, (2), pp. 216–226

[11] Fairall, E.W., Bilgin, B., Emadi, A.: 'State-of-the-art high-speed switched reluctance machines'. Proc. IEEE Int. Electric Machines & Drives Conf. (IEMDC), Coeur d'Alene, ID, USA, 2015, pp. 1621–1627

[12] Gong, C., Li, S., Habetler, T., *et al.*: 'Direct position control for ultrahigh-speed switched-reluctance machines based on low-cost nonintrusive reflective sensors', *IEEE Trans. Ind. Appl.*, 2019, **55**, (1), pp. 480–489

[13] Bostanci, E., Moallem, M., Parsapour, A., *et al.*: 'Opportunities and challenges of switched reluctance motor drives for electric propulsion: a comparative study', *IEEE Trans. Transp. Electr.*, 2017, **3**, (1), pp. 58–75

[14] Choi, Y.K., Yoon, H.S., Koh, C.S.: 'Pole-shape optimization of a switched-reluctance motor for torque ripple reduction', *IEEE Trans. Magn.*, 2007, **43**, (4), pp. 1797–1800

[15] Ma, C., Qu, L.: 'Multiobjective optimization of switched reluctance motors based on design of experiments and particle swarm optimization', *IEEE Trans. Energy Convers.*, 2015, **30**, (3), pp. 1144–1153

[16] Li, G., Ojeda, J., Hlioui, S., *et al.* 'Modification in rotor pole geometry of mutually coupled switched reluctance machine for torque ripple mitigating', *IEEE Trans. Magn.*, 2012, **48**, (6), pp. 2025–2034

[17] Vandana, R., Fernandes, B.G.: 'Design methodology for high-performance segmented rotor switched reluctance motors', *IEEE Trans. Energy Convers.*, 2015, **30**, (1), pp. 11–21

[18] Deng, X., Mecrow, B., Martin, R., *et al.*: 'Effects of winding connection on performance of a six-phase switched reluctance machine', *IEEE Trans. Energy Convers.*, 2018, **33**, (1), pp. 166–178

[19] Deng, X., Mecrow, B., Wu, H., *et al.*: 'Design and development of low torque ripple Variable-speed drive system with six-phase switched reluctance motors', *IEEE Trans. Energy Convers.*, 2018, **33**, (1), pp. 420–429

[20] Sun, Q., Wu, J., Gan, C., *et al.* 'A new phase current reconstruction scheme for four-phase SRM drives using improved converter topology without voltage penalty', *IEEE Trans. Ind. Electron.*, 2018, **65**, (1), pp. 133–144

[21] Chen, X., Wang, J., Patel, V.I., *et al.*: 'A nine-phase 18-slot 14-pole interior permanent magnet machine with low space harmonics for electric vehicle applications', *IEEE Trans. Energy Convers.*, 2016, **31**, (3), pp. 860–871

[22] Xu, S., Chen, H., Dong, F., *et al.*: 'Reliability analysis on power converter of switched reluctance machine system under different control strategies', *IEEE Trans. Ind. Electron.*, 2019, **66**, (8), pp. 6570–6580

[23] Chai, J.Y., Liaw, C.M.: 'Reduction of speed ripple and vibration for switched reluctance motor drive via intelligent current profiling', *IET Electr. Power Appl.*, 2010, **4**, (5), pp. 380–396

[24] Mikail, R., Husain, I., Sozer, Y., *et al.*: 'Torque-ripple minimization of switched reluctance machines through current profiling', *IEEE Trans. Ind. Appl.*, 2013, **49**, (3), pp. 1258–1267

[25] Xue, X.D., Cheng, K.W.E., Ho, S.L.: 'Optimization and evaluation of torque-sharing functions for torque ripple minimization in switched reluctance motor drives', *IEEE Trans. Power Electron.*, 2009, **24**, (9), pp. 2076–2090

[26] Ye, J., Bilgin, B., Emadi, A.: 'An offline torque sharing function for torque ripple reduction in switched reluctance motor drives', *IEEE Trans. Energy Convers.*, 2015, **30**, (2), pp. 726–735

[27] Li, H., Bilgin, B., Emadi, A.: 'An improved torque sharing function for torque ripple reduction in switched reluctance machines', *IEEE Trans. Power Electron.*, 2019, **34**, (2), pp. 1635–1644

[28] Inderka, R.B., De Doncker, R.W.: 'DITC-direct instantaneous torque control of switched reluctance drives', *IEEE Trans. Ind. Appl.*, 2003, **39**, (4), pp. 1046–1051

[29] Cheok, A.D., Fukuda, Y.: 'A new torque and flux control method for switched reluctance motor drives', *IEEE Trans. Power Electron.*, 2002, **17**, (4), pp. 543–557

[30] Sahoo, S.K., Dasgupta, S., Panda, S.K., *et al.*: 'A Lyapunov function-based robust direct torque controller for a switched reluctance motor drive system', *IEEE Trans. Power Electron.*, 2012, **27**, (2), pp. 555–564

[31] Ronanki, D., Williamson, S.S.: 'Comparative analysis of DITC and DTFC of switched reluctance motor for EV applications'. Proc. IEEE Int. Conf. on Industrial Technology (ICIT), Toronto, ON, Canada, 2017, pp. 509–514

[32] Pop, A.C., Petrus, V., Martis, C.S., *et al.*: 'Comparative study of different torque sharing functions for losses minimization in switched reluctance motors used in electric vehicles propulsion'. Proc. Int. Conf. on Optimization of Electrical and Electronic Equipment (OPTIM), Brasov, Romania, 2012, pp. 356–365

[33] Chancharoensook, P., Rahman, M.F.: 'Dynamic modeling of a four-phase 8/6 switched reluctance motor using current and torque look-up tables'. Proc.

28th Annual Conf. of the IEEE Industrial Electronics Society, Sevilla, Spain, 2002, pp. 491–496
[34] Ramanarayanan, V., Venkatesha, L., Panda, D.: 'Flux-linkage characteristics of switched reluctance motor'. Proc. IEEE Int. Conf. on Power Electronics, Drives and Energy Systems for Industrial Growth, New Delhi, India, 1996, pp. 281–285
[35] Song, Y., Wang, B.: 'Survey on reliability of power electronic systems', *IEEE Trans. Power Electron.*, 2013, **28**, (1), pp. 591–604
[36] Drofenik, U., Kolar, J.W.: 'A general scheme for calculating switching-and conduction-losses of power semiconductors in numerical circuit simulations of power electronic systems'. Proc. Int. Power Electronics Conf., Niigata, Japan, April 2005
[37] Wang, J., Zou, K., Chen, C., *et al.*: 'A high frequency battery model for current ripple analysis'. Proc. IEEE Applied Power Electronics Conf. and Exposition (APEC), Palm Springs, CA, USA, 2010, pp. 676–680

9 Appendix

SR motor specifications: rated power 4 kW, 8/6 pole (eight stator poles and six-rotor poles), 1500 rpm, r_j (phase resistance) = 0.7 Ω, L_u (unaligned inductance) = 12 mH, L_a (aligned inductance) = 110 mH, $J = 0.016\,\text{kg} - \text{m}^2$, $B = 0.0065$ N-ms.